International Tables for Crystallography (2006). Vol. C, Section 4.3.7, pp. 416–419.

standard matrix eigenvalue problem (for which efficient subroutines are widely available):

$$\sum_{\mathbf{h}} M_{\mathbf{gh}} C_{\mathbf{h}} = \gamma C_{\mathbf{g}}, \qquad (4.3.6.10)$$

where $M_{\mathbf{gh}} = U_{\mathbf{g}-\mathbf{h}}/2\chi + s_{\mathbf{g}}\delta_{\mathbf{gh}}$ and $s_{\mathbf{g}} = [k^2 - (\mathbf{k}+\mathbf{g})^2]/2\chi$ is the distance, measured in the z direction, of the reciprocal-lattice point $\mathbf{g}$ from the Ewald sphere.

There will in general be N distinct eigenvalues $\gamma = k_z - \chi_z$ corresponding to N possible values $k_z^{(j)}$, $j = 1, 2, \cdots N$, each with its eigenfunction defined by N wave amplitudes $C_0^{(j)}, C_{\mathbf{g}}^{(j)}, \ldots, C_{\mathbf{h}}^{(j)}$. The waves are normalized and orthogonal so that

$$\sum_{\mathbf{g}} C_{\mathbf{g}}^{(j)*} C_{\mathbf{g}}^{(l)} = \delta_{jl}; \quad \sum_{j} C_{\mathbf{g}}^{(j)*} C_{\mathbf{h}}^{(l)} = \delta_{\mathbf{gh}}. \qquad (4.3.6.11)$$

In simple transmission geometry, the complete solution for the total coherent wavefunction $\psi(\mathbf{r})$ is

$$\psi(\mathbf{r}) = \sum_{j} \psi^{(j)} \exp[-2\pi q^{(j)} z] \sum_{\mathbf{g}} C_{\mathbf{g}}^{(j)} \exp[2\pi i (\chi + \mathbf{g}) \cdot \mathbf{r}]. \qquad (4.3.6.12)$$

Inelastic and thermal-diffuse-scattering processes cause anomalous absorption effects whereby the amplitude of each component Bloch wave decays with depth z in the crystal from its initial value $\psi^{(j)} = C_0^{(j)*}$. The decay constant is computed using an imaginary optical potential $iU'(\mathbf{r})$ with Fourier coefficients $iU'_{\mathbf{g}} = iU'^{*}_{-\mathbf{g}}$ (for further details of these see Humphreys & Hirsch, 1968, and Subsection 4.3.1.5 and Section 4.3.2).

$$q^{(j)} = \frac{m}{h^2 \chi_z} \sum_{\mathbf{g},\mathbf{h}} C_{\mathbf{g}}^{(j)*} U'_{\mathbf{h}} C_{\mathbf{g}-\mathbf{h}}^{(j)}. \qquad (4.3.6.13)$$

The Bloch-wave, matrix-diagonalization method has been extended to include reciprocal-lattice points in higher-order Laue zones (Jones, Rackham & Steeds, 1977) and, using pseudopotential scattering amplitudes, to the case of low-energy electrons (Pendry, 1974).

The Bloch-wave picture may be compared with other variants of dynamical diffraction theory, which, like the multislice method (Subsection 4.3.6.1), for example, employ plane waves whose amplitudes vary with position in real space and are determined by numerical integration of first-order coupled differential equations. For cases with $N < 50$ beams in perfect crystals or in crystals containing localized defects such as stacking faults or small point-defect clusters, the Bloch-wave method offers many advantages, particularly in thicker crystals with $t > 1000$ Å. For high-resolution image calculations in thin crystals where the periodic continuation process may lead to several hundred diffracted beams, the multislice method is more efficient. For cases of defects with extended strain fields or crystals illuminated at oblique incidence, coupled plane-wave integrations along columns in real space (Howie & Basinski, 1968) can be the most efficient method.

The general advantage of the Bloch-wave method, however, is the picture it affords of wave propagation and scattering in both perfect and imperfect crystals. For this purpose, solutions of equations (4.3.6.9) allow dispersion surfaces to be plotted in k space, covering with several sheets j all the wave points $\mathbf{k}^{(j)}$ for a given energy E. Thickness fringes and other interference effects then arise because of interference between waves excited at different points $\mathbf{k}^{(j)}$. The average current flow at each point is normal to the dispersion surface and anomalous-absorption effects can be understood in terms of the distribution of Bloch-wave current within the unit cell. Detailed study of these effects, and the behaviour of dispersion surfaces as a function of energy, yields accurate data on scattering amplitudes *via* the critical-voltage effect (see Section 4.3.7). Static crystal defects induce elastic scattering transitions $\mathbf{k}^{(j)} \to \mathbf{k}^{(l)}$ on sheets of the same dispersion surface. Transitions between points on dispersion surfaces of different energies occur because of thermal diffuse scattering, generation of electronic excitations or the emission of radiation by the fast electron. The Bloch-wave picture and the dispersion surface are central to any description of these phenomena. For further information and references, the reader may find it helpful to consult Section 5.2.10 of Volume B (*IT* B, 1996).

4.3.7. Measurement of structure factors and determination of crystal thickness by electron diffraction (by J. Gjønnes and J. W. Steeds)

Current advances in quantitative electron diffraction are connected with improved experimental facilities, notably the combination of convergent-beam electron diffraction (CBED) with new detection systems. This is reflected in extended applications of electron diffraction intensities to problems in crystallography, ranging from valence-electron distributions in crystals with small unit cells to structure determination of biological molecules in membranes. The experimental procedures can be seen in relation to the two main principles for measurement of diffracted intensities from crystals:

– *rocking curves*, *i.e.* intensity profiles measured as function of deviation, s_g, from the Bragg condition, and

– *integrated intensities*, which form the well known basis for X-ray and neutron diffraction determination of crystal structure.

Integrated intensities are not easily defined in the most common type of electron-diffraction pattern, *viz* the selected-area (SAD) spot pattern. This is due to the combination of dynamical scattering and the orientation and thickness variations usually present within the typically micrometre-size illuminated area. This combination leads to spot pattern intensities that are poorly defined averages over complicated scattering functions of many structure factors. Convergent-beam electron diffraction is a better alternative for intensity measurements, especially for inorganic structures with small-to-moderate unit cells. In CBED, a fine beam is focused within an area of a few hundred ångströms, with a divergence of the order of a tenth of a degree. The diffraction pattern then appears in the form of discs, which are essentially two-dimensional rocking curves from a small illuminated area, within which thickness and orientation can be regarded as constant. These intensity distributions are obtained under well defined conditions and are well suited for comparison with theoretical calculations. The intensity can be recorded either photographically, or with other parallel recording systems, *viz* YAG screen/CCD camera (Krivanek, Mooney, Fan, Leber & Meyer, 1991) or image plates (Mori, Oikawa & Harada, 1990) – or sequentially by a scanning system. The inelastic background can be removed by an energy filter (Krahl, Pätzold & Swoboda,1990; Krivanek, Gubbens, Dellby & Meyer, 1991). Detailed intensity profiles in one or two dimensions can then be measured with high precision for low-order reflections from simple structures. But there are limitations also with the CBED technique: the crystal should be fairly perfect within the illuminated area and the unit cell relatively small, so that overlap between discs can be avoided. The current development of electron diffraction is therefore characterized by a wide range of techniques, which extend from the traditional spot pattern to two-dimensional, filtered rocking curves, adapted to the

Copyright © 2006 International Union of Crystallography

structure problems under study and the specimens that are available.

Spot-pattern intensities are best for thin samples of crystals with light atoms, especially organic and biological materials. Dorset and co-workers (Dorset, Jap, Ho & Glaeser, 1979; Dorset, 1991) have shown how conventional crystallographic techniques ('direct phasing') can be applied in *ab initio* structure determination of thin organic crystals from spot intensities in projections. Two main complications were treated by them: bending of the crystal and dynamical scattering. Thin crystals will frequently be bent; this will give some integration of the reflection, but may also produce a slight distortion of the structure, as pointed out by Cowley (1961), who proposed a correction formula. The thickness range for which a kinematical approach to intensities is valid was estimated theoretically by Dorset *et al.* (1979). For organic crystals, they quoted a few hundred ångströms as a limit for kinematical scattering in dense projections at 100 kV.

Radiation damage is a problem, but with low-dose and cryo-techniques, electron-microscopy methods can be applied to many organic crystals, as shown by several recent investigations. Voigt-Martin, Yan, Gilmore, Shankland & Bricogne (1994) collected electron-diffraction intensities from a beam-sensitive dione and constructed a 1.4 Å Fourier map by a direct method based on maximum entropy. Large numbers of electron-diffraction intensities have been collected from biological molecules crystallized in membranes. The structure amplitudes can be combined with phases extracted from high-resolution micrographs, following Unwin & Henderson's (1975) early work. Kühlbrandt, Wang & Fujiyoshi (1994) collected about 18 000 amplitudes and 15 000 phases for a protein complex in an electron cryomicroscope operating at 4.2 K (Fujiyoshi *et al.*, 1991). Using these data, they determined the structure from a three-dimensional Fourier map calculated to 3.4 Å resolution. The assumption of kinematical scattering in such studies has been investigated by Spargo (1994), who found the amplitudes to be kinematic within 4% but with somewhat larger deviations for phases.

For inorganic structures, spot-pattern intensities are less useful because of the stronger dynamical interactions, especially in dense zones. Nevertheless, it may be possible to derive a structure and refine parameters from spot-pattern intensities. Andersson (1975) used experimental intensities from selected projections for comparison with dynamical calculations, including an empirical correction factor for orientation spread, in a structure determination of $V_{14}O_8$. Recently, Zou, Sukharev & Hovmöller (1993) combined spot-pattern intensities read from film by the program *ELD* with image processing of high-resolution micrographs for structure determination of a complex perovskite.

A considerable improvement over the spot pattern has been obtained by the elegant double-precession technique devised by Vincent & Midgley (1994). They programmed scanning coils above and below the specimen in the electron microscope so as to achieve simultaneous precession of the focused incident beam and the diffraction pattern around the optical axis. The net effect is equivalent to a precession of the specimen with a stationary incident beam. Integrated intensities can be obtained from reflections out to a Bragg angle θ equal to the precession angle φ for the zeroth Laue zone. In addition, reflections in the first and second Laue zones appear as broad concentric rings. Dynamical effects are reduced appreciably by this procedure, especially in the non-zero Laue zones. The experimental integrated intensities, I_g, must be multiplied with a geometrical factor analogous to the Lorentz factor in X-ray diffraction, *viz*

$$I_g = I_G^{\rm exp} \sin\varepsilon; \quad \cos\varepsilon = \frac{(g^2 - 2nkh)}{2k\phi g}, \qquad (4.3.7.1)$$

where nh is the reciprocal spacing between the zeroth and nth layers. The intensities can be used for structure determination by procedures taken over from X-ray crystallography, *e.g.* the conditional Patterson projections that are used by the Bristol group (Vincent, Bird & Steeds, 1984). The precession method may be seen as intermediate between the spot pattern and the CBED technique. Another intermediate approach was proposed by Goodman (1976) and used later by Olsen, Goodman & Whitfield (1985) in the structure determination of a series of selenides. CBED patterns from thin crystals were taken in dense zones; intensities were measured at corresponding points in the discs, *e.g.* at the zone-axis position. Structure parameters were determined by fitting the observed intensities to dynamical calculations.

Higher precision and more direct comparisons with dynamical scattering calculations are achieved by measurements of intensity distributions within the CBED discs, *i.e.* one- or two-dimensional rocking curves. An up-to-date review of these techniques is found in the recent book by Spence & Zuo (1992), where all aspects of the CBED technique, theory and applications are covered, including determination of lattice constants and strains, crystal symmetry, and fault vectors of defects. Refinement of structure factors in crystals with small unit cells are treated in detail. For determination of bond charges, the structure factors (Fourier potentials) should be determined to an accuracy of a few tenths of a percent; calculations must then be based on many-beam dynamical scattering theory, see Chapter 8.8. Removal of the inelastic background by an energy filter will improve the data considerably; analytical expressions for the inelastic background including multiple-scattering contributions may be an alternative (Marthinsen, Holmestad & Høier, 1994).

Early CBED applications to the determination of structure factors were based on features that can be related to dynamical effects in the two-beam case. Although insufficient for most accurate analyses, the two-beam expression for the intensity profile may be a useful guide. In its standard form,

$$I_g(s) = \frac{(U_g/k)^2}{s_g^2 + (U_g/k)^2} \sin^2\left[\pi t \sqrt{s_g^2 + (U_g/k)^2}\right], \qquad (4.3.7.2)$$

where U_g and s_g are Fourier potential and excitation error for the reflection g, k wave number and t thickness. The expression can be rewritten in terms of the eigenvalues $\gamma^{(i,j)}$ that correspond to the two Bloch-wave branches, i, j:

$$I_g^{i,j}(s_g) = \frac{(U_g/k)^2}{(\gamma^{(i)} - \gamma^{(j)})^2} \sin^2[\pi t(\gamma^{(i)} - \gamma^{(j)})], \qquad (4.3.7.3)$$

where

$$\gamma^{i,j} = \tfrac{1}{2}\left[s_g^2 \pm \sqrt{s_g^2 + (U_g/k)^2}\,\right].$$

Note that the minimum separation between the branches i,j or the gap at *the dispersion surface* is

$$(\gamma^{(j)} - \gamma^{(i)})_{\rm min} = U_g/k = 1/\xi_g, \qquad (4.3.7.4)$$

where ξ_g is an extinction distance. The two-beam form is often found to be a good approximation to an intensity profile $I_g(s_g)$ even when other beams are excited, provided an *effective potential* $U_g^{\rm eff}$, which corresponds to the gap at the dispersion surface, is substituted for U_g. This is suggested by many features in CBED and Kikuchi patterns and borne out by detailed calculations, see *e.g.* Høier (1972). Approximate expressions for

$U_g^{\rm eff}$ have been developed along different lines; the best known is the Bethe potential

$$U_g^{\rm eff} = U_g - \sum_h \frac{U_{g-h}U_h}{2ks_h}. \qquad (4.3.7.5)$$

Other perturbation approaches are based on scattering between Bloch waves, in analogy with the 'interband scattering' introduced by Howie (1963) for diffuse scattering; the term 'Bloch-wave hybridization' was introduced by Buxton (1976). Exact treatment of symmetrical few-beam cases is possible (see Fukuhara, 1966; Kogiso & Takahashi, 1977). The three-beam case (Kambe, 1957; Gjønnes & Høier 1971) is described in detail in the book by Spence & Zuo (1992).

Many intensity features can be related to the structure of the dispersion surface, as represented by the function $\gamma(k_x,k_y)$. The gap [equation (4.3.7.4)] is an important parameter, as in the four-beam symmetrical case in Fig. 4.3.7.1. Intensity measurements along one dimension can then be referred to three groups, according to the width of the gap, *viz*:

small gap – integrated intensity;
large gap – rocking curve, thickness fringes;
zero gap – critical effects.

A small gap at the dispersion surface implies that the two-beam-like rocking curve above approaches a kinematical form and can be represented by an integrated intensity. Within a certain thickness range, this intensity may be proportional to $|U_g^{\rm eff}|^2$, with an angular width inversely proportional to gt. Several schemes have been proposed for measurement of relative integrated intensities for reflections in the outer, high-angle region, where the lines are narrow and can be easily separated from the background. Steeds (1984) proposed use of the HOLZ (high-order Laue-zone) lines, which appear in CBED patterns taken with the central disc at the zone-axis position. Along a ring that defines the first-order Laue zone (FOLZ), reflections appear as segments that can be associated with scattering from strongly excited Bloch waves in the central ZOLZ part into the FOLZ reflections. Vincent, Bird & Steeds (1984) proposed an intensity expression

$$I_g^{(j)} \propto |\varepsilon^{(j)}\beta_g^{(j)}|^2 \exp(-2\mu t)\frac{1-\exp[-2(\mu^{(j)}-\mu)t]}{2(\mu^{(j)}-\mu)} \qquad (4.3.7.6)$$

for integrated intensity for a line segment associated with scattering from (or into) the ZOLZ Bloch wave j. $\varepsilon^{(j)}$ is here the excitation coefficient and $\beta^{(j)}$ the matrix element for scattering between the Bloch wave j and the plane wave g. $\mu^{(j)}$ and μ are absorption coefficients for the Bloch wave and plane wave, respectively; t is the thickness. From measurements of a number of such FOLZ (or SOLZ) reflections, they were able to carry out *ab initio* structure determinations using so-called conditional Patterson projections and coordinate refinement. Tanaka & Tsuda (1990) have refined atomic positions from zone-axis HOLZ intensities. Ratios between HOLZ intensities have been used for determination of the Debye–Waller factor (Holmestad, Weickenmeier, Zuo, Spence & Horita, 1993).

Another CBED approach to integrated intensities is due to Taftø & Metzger (1985). They measured a set of high-order reflections along a systematic row with a wide-aperture CBED tilted off symmetrical incidence. A number of high-order reflections are then simultaneously excited in a range where the reflections are narrow and do not overlap. Gjønnes & Bøe (1994) and Ma, Rømming, Lebech & Gjønnes (1992) applied the technique to the refinement of coordinates and thermal parameters in high-T_c superconductors and intermetallic compounds. The validity and limitation of the kinematical approximation and dynamic potentials in this case has been discussed by Gjønnes & Bøe (1994).

Zero gap at the dispersion surface corresponds to zero effective Fourier potential or, to be more exact, an accidental degeneracy, $\gamma^{(i)} = \gamma^{(j)}$, in the Bloch-wave solution. This is the basis for the critical-voltage method first shown by Watanabe, Uyeda & Fukuhara (1969). From vanishing contrast of the Kikuchi line corresponding to a second-order reflection $2g$, they determined a relation between the structure factors U_g and U_{2g}. Gjønnes & Høier (1971) derived the condition for the accidental degeneracy in the general centrosymmetrical three-beam case $0,g,h$, expressed in terms of the excitation errors $s_{g,h}$ and Fourier potentials $U_{g,h,g-h}$, *viz*

$$2ks_g = \frac{U_g(U_h^2 - U_{g-h}^2)m}{U_hU_{g-h}m_0}; \quad 2ks_h = \frac{U_h(U_g^2 - U_{g-h}^2)m}{U_gU_{g-h}m_0}; \qquad (4.3.7.7)$$

where m and m_0 are the relativistic and rest mass of the incident electron. Experimentally, this condition is obtained at a particular voltage and diffraction condition as vanishing line contrast of a Kikuchi or Kossel line – or as a reversal of a contrast feature. The second-order critical-voltage effect is then obtained as a special case, *e.g.* by the mass ratio:

$$(m/m_0)_{\rm crit} = \frac{U_{2h}h^2}{U_h^2 - U_{2h}^2}. \qquad (4.3.7.8)$$

Measurements have been carried out for a number of elements and alloy phases; see the review by Fox & Fisher (1988) and later work on alloys by Fox & Tabbernor (1991). Zone-axis critical voltages have been used by Matsuhata & Steeds (1987). For analytical expressions and experimental determination of non-systematic critical voltages, see Matsuhata & Gjønnes (1994).

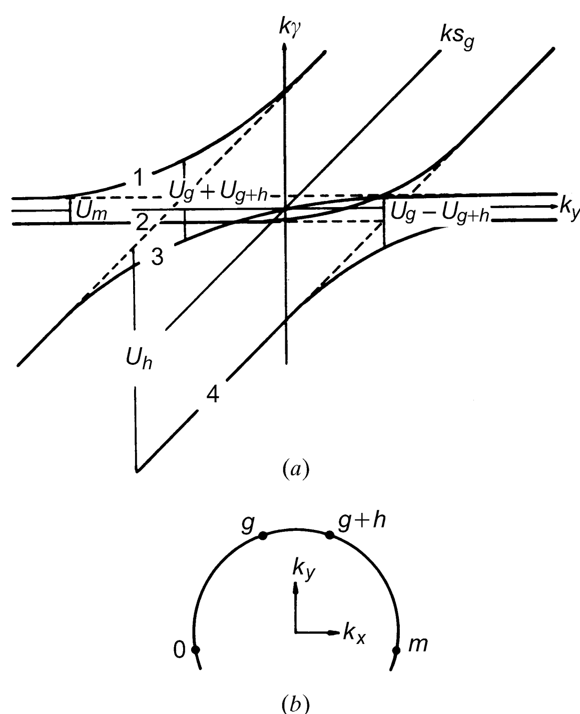

Fig. 4.3.7.1. (*a*) Dispersion-surface section for the symmetric four-beam case (0, g, $g+h$, m), γk is a function of k_x, referred to (*b*), where $k_x = k_y = 0$ corresponds to the exact Bragg condition for all three reflections. The two gaps appear at $s_g = \pm(U_h - U_m)/k$ with widths $(U_g \pm U_{g+h})/k$.

Large gaps at the dispersion surface are associated with strong inner reflections – and a strong dynamical effect of two-beam-like character. The absolute magnitude of the gap – or its inverse, the extinction distance – can be obtained in different ways. Early measurements were based on the split of diffraction spots from a wedge, see Lehmpfuhl (1974), or the corresponding fringe periods measured in bright- and dark-field micrographs (Ando, Ichimiya & Uyeda, 1974). The most precise and applicable large-gap methods are based on the refinement of the fringe pattern in CBED discs from strong reflections, as developed by Goodman & Lehmpfuhl (1967) and Voss, Lehmpfuhl & Smith (1980). In recent years, this technique has been developed to high perfection by means of filtered CBED patterns, see Spence & Zuo (1992) and papers referred to therein. See also Chapter 8.8.

The gap at the dispersion surface can also be obtained directly from the split observed at the crossing of a weak Kikuchi line with a strong band. Gjønnes & Høier (1971) showed how this can be used to determine strong low-order reflections. High voltage may improve the accuracy (Terasaki, Watanabe & Gjønnes, 1979). The sensitivity of the intersecting Kikuchi-line (IKL) method was further increased by the use of CBED instead of Kikuchi patterns (Matsuhata, Tomokiyo, Watanabe & Eguchi, 1984; Taftø & Gjønnes, 1985). In a recent development, Høier, Bakken, Marthinsen & Holmestad (1993) have measured the intensity distribution in the CBED discs around such intersections and have refined the main structure factors involved.

Two-dimensional rocking curves collected by CBED patterns around the axis of a dense zone are complicated by extensive many-beam dynamical interactions. The Bristol–Bath group (Saunders, Bird, Midgley & Vincent, 1994) claim that the strong dynamic effects can be exploited to yield high sensitivity in refinement of low-order structure factors. They have also developed procedures for *ab initio* structure determination based on zone-axis patterns (Bird & Saunders, 1992), see Chapter 8.8.

Determination of phase invariants. It has been known for some time (*e.g* Kambe, 1957) that the dynamical three-beam case contains information about phase. As in the X-ray case, measurement of dynamical effects can be used to determine the value of triplets (Zuo, Høier & Spence, 1989) and to determine phase angles to better than one tenth of a degree (Zuo, Spence, Downs & Mayer, 1993) which is far better than any X-ray method. Bird (1990) has pointed out that the phase of the absorption potential may differ from the phase of the real potential.

Thickness is an important parameter in electron-diffraction experiments. In structure-factor determination based on CBED patterns, thickness is often included in the refinement. Thickness can also be determined directly from profiles connected with large gaps at the dispersion surface (Goodman & Lehmpfuhl, 1967; Blake, Jostsons, Kelly & Napier, 1978; Glazer, Ramesh, Hilton & Sarikaya, 1985). The method is based on the outer part of the fringe profile, which is not so sensitive to the structure factor. The intensity minimum of the ith fringe in the diffracted disc occurs at a position corresponding to the excitation error s_i and expressed as

$$(s_i^2 + 1/\varepsilon_g^2)t^2 = n_i^2, \qquad (4.3.7.9)$$

where n_i is a small integer describing the order of the minimum. This equation can be arranged in two ways for graphic determination of thickness. The commonest method appears to be to plot $(s_i/n_i)^2$ against $1/n_i^2$ and then determine the thickness from the intersection with the ordinate axis (Kelly, Jostsons, Blake & Napier, 1975). Glazer *et al.* (1985) claim that the method originally proposed by Ackermann (1948), where s_i^2 is plotted against n_i and the thickness is taken from the slope, is more accurate. In both cases, the outer part of the rocking curve is emphasized; exact knowledge of the gap is not necessary for a good determination of thickness, provided the assumption of a two-beam-like rocking curve is valid.

4.3.8. Crystal structure determination by high-resolution electron microscopy (By J. C. H. Spence and J. M. Cowley)

4.3.8.1. *Introduction*

For the crystallographic study of real materials, high-resolution electron microscopy (HREM) can provide a great deal of information that is complementary to that obtainable by X-ray and neutron diffraction methods. In contrast to the statistically averaged information that these other methods provide, the great power of HREM lies in its ability to elucidate the detailed atomic arrangements of individual defects and the microcrystalline structure in real crystals. The defects and inhomogeneities of real crystals frequently exert a controlling influence on phase-transition mechanisms and more generally on all the electrical, mechanical, and thermal properties of solids. The real-space images that HREM provides (such as that shown in Fig. 4.3.8.1) can give an immediate and dramatic impression of chemical crystallography processes, unobtainable by other methods. Their atomic structure is of the utmost importance for

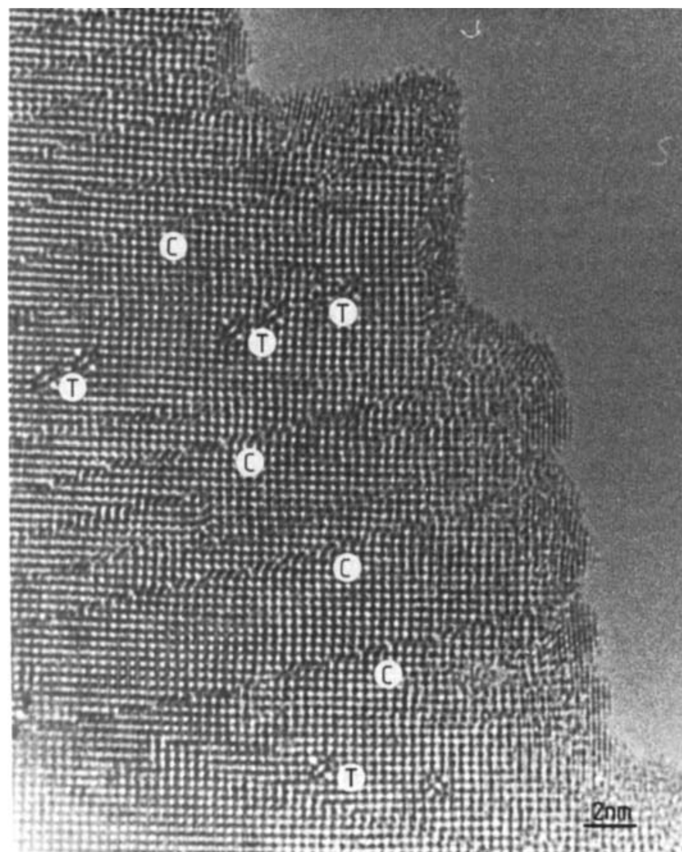

Fig. 4.3.8.1. Atomic resolution image of a tantalum-doped tungsten trioxide crystal (pseudo-cubic structure) showing extended crystallographic shear-plane defects (C), pentagonal-column hexagonal-tunnel (PCHT) defects (T), and metallization of the surface due to oxygen desorption (JEOL 4000EX, crystal thickness less than 200 Å, 400 kV, $C_s = 1$ mm). Atomic columns are black. [Smith, Bursill & Wood (1985).]

references